

Supplementary Information for

Environmental drivers of water use for Caatinga woody plant species: combining remote sensing phenology and sap flow measurements

Rennan A. Paloschi, Desirée Marques Ramos, Dione J. Ventura, Rodolfo Souza, Eduardo Souza, Leonor Patrícia Cerdeira Morellato, Rodolfo L. B. Nóbrega, Ítalo Antônio Cotta Coutinho, Anne Verhoef, Thales Sehn Körting and Laura S. Borma

Rennan A. Paloschi.

E-mail: rennan.paloschi@inpe.br

This PDF file includes:

Supplementary text

Figs. S1 to S2

Tables S1 to S2

SI References

Supporting Information Text

Subhead. Type or paste text here. This should be additional explanatory text such as an extended technical description of results, full details of mathematical models, etc.

1. Supplementary Materials and Methods

A. Meteorological data. Meteorological variables for this study were collated from May onwards. The variables analyzed were rainfall (P), evapotranspiration, ET, Net radiation (R_n), air temperature (T_{air}) and vapor pressure deficit, VPD. Rainfall was measured with a rain gauge (TE525WS-L, Texas Electronics, Dallas, TX, USA). R_n was measured with a net radiometer (NRLITE, Kipp & Zonen, Delft, Netherlands). To calculate ecosystem ET, half-hourly turbulent fluxes of latent heat (LE) above the canopy were measured continuously using the EC technique consisting of a three-dimensional sonic anemometer (model CSAT3, Campbell Scientific Inc., Logan, UT, USA) and a fast-response $\text{CO}_2/\text{H}_2\text{O}$ infrared gas analyzer (model LI7500DS LI-COR Inc., Lincoln, NE USA). The raw data were recorded at a rate of 10 Hz and processed using the software EddyPro v. 7.0.4 (LI-COR Inc.) where coordinate rotation and Webb-Pearman-Leuning corrections were performed. The gaps in the dataset, due to system malfunctions, extreme rain events, and power failures, were filled using the REdDyProc package (1), using the R programming language (2). For more details about site instrumentation, please see (3).

B. Soil moisture and soil matric potential. To monitor soil moisture and soil matric potential, we installed inside the monitoring plot (Figure 1), three profiles of soil moisture sensors (5TM, Decagon Devices, Pullman, WA, USA), with the sensors located at 5, 15, 25, 40 and 65 cm depths. In one of these profiles, five matric potential sensors (MPS-6, Decagon Devices, Pullman, WA, USA) were installed at the same depths as the soil moisture sensors. Data were recorded every 20 minutes on a self-manufactured data logger based on the Arduino Platform, powered by solar panels and batteries and programmed with the standard calibration equation that describes the relationship between the dielectric constant and volumetric soil moisture content for mineral soils (4), recommended by Decagon Devices (5).

The total profile soil moisture content (θ_{prof}) was computed taking into account the thickness of the soil layer represented by each sensor. Each sensor was assumed to be at the center of a layer that started and ended half-way in between the two nearest sensors. The distance between these pairs of sensors defined the thickness of the layers, which was multiplied with the soil moisture content and summed, generating a total soil moisture storage value for each profile. So, despite the fact that the deepest sensor was installed at 65 cm soil depth, the total depth of the monitored soil moisture profile was 77.5 cm. Subsequently, the values of the three profiles were averaged to obtain a single total soil moisture storage value for the monitoring plot (S_w), also expressed in mm of water.

As the soil dries, roots need to apply a higher 'suction' to extract water from the soil. Thus, the plant's capacity to extract water from the soil is more closely related to the soil matric potential (with the term 'suction' denoting the absolute value of the matric potential) than to the volumetric water content (θ , $\text{m}^3 \text{m}^{-3}$) (6). The relationship between the moisture content retained in the soil, θ , and its concurrent matric potential, Ψ , (the so-called soil water retention curve, WRC) depends on the structural characteristics of the soil (as determined by texture and pore-size distribution). This curve can be constructed from laboratory or field measurements, and its shape subsequently described by a mathematical model equation that fits the WRC. For this study, the equations that describe the WRCs for each depth, based on field observed data of θ and Ψ , were determined with the Durner model (7), using the software SWRC Fit (8). To avoid the hysteresis effect, we only used data (θ and Ψ) for periods when the soil was drying out.

Durner's equation is given by

$$S_e = \sum_{i=1}^k W_i \left[\frac{1}{1 + (\alpha_i |\Psi|)^{n_i}} \right]^{m_i} \quad [1]$$

where S_e is the relative saturation (dependent on the actual θ , the residual moisture content, θ_r , and the saturated moisture content, θ_s , see Eq. 2), Ψ is the suction, α_i and n_i are curve fitting parameters (where m_i is derived from n_i), k is the number of "subsystems" that form the total pore-size distribution, and W_i are weighting factors for the sub-curves, subject to $0 < W_i < 1$ and $\sum W_i = 1$. For the present study $k = 2$ was used (bi-modal pore-system), separating between micro- and mesopore flow, and macropore flow. Parameter W_i was found to range from 0.32 to 0.85, depending on the soil layer.

Next, θ_r and θ_s values for each layer, fitted parameters of the Durner equation, were used to calculate a layer thickness-weighted profile-average $\theta_{r,prof}$ and $\theta_{s,prof}$. Together with the profile averaged volumetric soil moisture, θ_{prof} , these values were used to calculate the relative saturation of the entire soil profile ($S_{e,prof}$):

$$S_{e,prof} = \frac{\theta_{prof} - \theta_{r,prof}}{\theta_{s,prof} - \theta_{r,prof}} \quad [2]$$

In the paper, the data presentation and discussion were conducted in terms of the relative saturation ($S_{e,prof}$), because it allows for a better comparison among sites. In Table S1, we also provide the values for plant wilting point (θ_{wp} ; $\text{m}^3 \text{m}^{-3}$) and field capacity (θ_{fc} ; $\text{m}^3 \text{m}^{-3}$) because this information can be useful to other researchers working on Caatinga vegetation, and related soil environment. They were derived from the fitted WRCs, using Eq. 2, for each soil depth, considering θ_{fc} as the soil moisture at a matric potential of 10 kPa, and θ_{wp} as the soil moisture at a matric potential of 1500 kPa. These values were also profile-averaged, following the procedure presented above.

A perhaps more meaningful normalization of the volumetric soil moisture content would be achieved using θ_{fc} and θ_{wp} (6), as their difference theoretically represents the soil moisture range over which vegetation can extract water from soil, i.e., the plant-available water; this normalized soil moisture content is called the fraction of transpirable soil water (FTSW). However, since in the measured timeseries there are θ_{prof} values lower than soil profile soil moisture content at wilting point (θ_{wpp}) (Table S1), it would result in negative values of FTSW (see Eq. 2). Zeroing the negative values, as suggested by (9), would be inappropriate in our case, since the period corresponding to the driest part of the dataset is important in the context of our research questions, e.g. in relation to the (rate of) response of the vegetation at the beginning of a new rainy season to the initial increase in soil moisture content.

C. Sap flow data. Sap flow was measured in twenty plant individuals belonging to the five different tree species selected (see Experimental strategy); The sap flux density (F_d , $g\ m^{-2}\ min^{-1}$) was measured using Granier’s TDP method. Two probes were installed in the tree trunk, separated by 10-15 cm, and in contact with the xylem. The sensors were covered with reflective insulation to reduce the influence of direct sunlight on thermal gradients. The upper probe was equipped with an electric resistance, heated at a constant power, while the lower probe remained at tree temperature. The working principle is that the sap flow cools the upper probe, thereby decreasing the temperature difference between the heated and non-heated probes (ΔT , $^{\circ}C$), so that F_d is inversely proportional to the temperature difference. Sap flow density is empirically given by (10):

$$F_d = 118.99 \times 10^{-6} [(\Delta T_{max} - \Delta T) / \Delta T]^{1.231} \quad [3]$$

where ΔT_{max} corresponds to the maximum temperature difference (determined as per the procedure detailed below), for which $F_d = 0$.

Due to changes in the thermal equilibrium conditions of the xylem, ΔT_{max} may differ between days and hence will vary throughout the monitoring period (11). In our study, the value of ΔT_{max} was assumed to equal the maximum value of ΔT registered by the sap flow system during the nocturnal period of each day (i.e. 22h00 to 4h00; UTC-3 Universal Time Coordinated). For the days where power failures occurred during the night, the night value of the previous day was considered. An average value of F_d per species was calculated (by averaging values for the four individuals) and this species-average was normalized from 0 to 1 taking into account the minimum and maximum F_d for each species; this normalized average for each species is referred to in this study as F_{dn} .

In this study, we considered only the intra-annual course of sap flow and not the exact amount of water used. Therefore, for analysis of the relationship between sap flow and measured environmental variables only the typical flow density of the morning period, at 10h30 (UTC-3), was considered as representative of the flow of the day. The choice of 10h30 was not entirely arbitrary, since i) this time is close to the MODIS Terra and Sentinel-2 overpass time, and ii) the sap flow at this time of the day exhibits a very strong correlation with the total daily sap flow – so that it represents an approximate estimate of daily water use.

To represent the community-scale transpiration of the monitoring plot, a weighted average was calculated, for which we considered the sapwood contribution by each species. The total amount of plot transpiration was normalized between 0 and 1, and referred to in this paper as normalized flux density of the monitored species community (F_{dnc}).

The total sapwood area for all individuals belonging to the monitored plant species was estimated based on the linear relationship between the radial diameter of the sapwood and the diameter at breast height (DBH) (12). Cylindrical cross section samples were collected from all monitored trees using a drill typically used for dendrochronology. The sapwood area of the samples was measured using dye-aided visual analysis. Despite the issues reported by some authors (13), this simple technique is cheap and objective, yielding results that are appropriated for the proposed analysis. Because there was not enough variation in trunk diameter to estimate a dendrometric relationship for each species, the same linear equation was derived to estimate the sapwood of all five monitored species. The sapwood area was calculated for each individual using the estimated sapwood radial diameter and the standard equation used to calculate the area of a circle, by subtraction of the estimated core area and estimated bark area from the total measured tree cross sectional area.

D. Near-surface and Orbital Remote Sensing, RS. The RGB chromatic coordinates (RGBcc) indices are the most suitable type of index to detect leaf color changes, such as changes caused by leaf development and photosynthetic dynamics, and the most efficient type of index to minimise the effects of light variations (14–19). A great advantage of this approach is that it can be extracted from ordinary cameras, which normally only cover the RGB spectrum. In this study, the green chromatic coordinate (GCC) was calculated according to the following equation:

$$GCC = \frac{Green_{avg}}{Red_{avg} + Green_{avg} + Blue_{avg}} \quad [4]$$

To obtain the individual GCC, a downward facing digital hemispherical Mobotix Q 25 lens camera (Mobotix AG-Germany) was placed in the EC flux tower attached to an extension arm facing south (northeast of the monitoring plot) at a vertical distance of 6m from the top of the canopy. The camera was powered by a 12 V battery that was charged by solar panels. The camera was set to automatically take a sequence of five JPEG images (at 1280 X 960 pixels of resolution) in the first 10 minutes of each hour, from 6h00 to 18h00 (UTC-3), on a daily basis, as described in (15, 20).

Field surveys were conducted to identify and compile a list of the main plant species captured by the field of view of the camera. Next, the identified individuals were matched with the crowns observed in the images. Raw images were initially

screened visually to remove photographs where the images were saturated, too dark, showed evidence of some digital registration failure, or when the lens had been removed for cleaning. The remaining images were analyzed in terms of the contribution of the relative brightness of red, green, and blue color channels (RGBcc; (19)), as described by (14, 16, 18, 20).

Furthermore, in order to capture the community-wide phenological response through the use of satellite data, the Normalized Difference Vegetation Index - NDVI was used, computed by the normalized difference between the reflectance in the red (Red) and near infrared (NIR) parts of the spectrum:

$$NDVI = \frac{NIR - Red}{NIR + Red} \quad [5]$$

The NDVI derived from orbital images was obtained by using data from two different satellite missions, each with different spatiotemporal resolutions. The one with the highest spatial resolution and a relatively recent launch date concerns the Sentinel-2 A and B satellites, S2-A and S2-B, respectively. The second multi-spectral data source relates to an already consolidated and widely used sensor, the Moderate-Resolution Imaging Spectroradiometer (MODIS), aboard the Terra and Aqua satellites; this sensor has an acquisition frequency of 1 day. Sentinel-2 satellites provide a 10-60 m spatial resolution, with a revisit time varying from 3 to 10 days. For the MODIS sensor, we used the NDVI provided by the MOD13Q1 and MYD13Q1 products (21, 22), made available by the National Aeronautics and Space Administration (NASA). The MOD13Q1 and MYD13Q1 consist of images composed by the best quality pixels of the daily NDVI, observed in a 16-days compilation, with 250-m spatial resolution. Thus, different pixels present in the same NDVI image composition may have been acquired on different days. Instead, we considered the acquisition date of each pixel and not the composition date.

For the correlation analyses with the sap flux density, F_{dnc} values at 10:30 am were compared with the values of the orbital satellites at the same time and on the same day. The Sentinel-2 images were corrected to represent surface reflectance using the sen2cor plugin that is part of the Snap software. A cloud filter was applied using Google Earth Engine using the cloud mask generated by the sen2cor plugin; however, a second visual analysis was necessary because some cloudy images were not automatically detected by the algorithm.

The NDVI was calculated from the following two bands (665 and 842 nm, Red-B4 and NIR-B8, respectively) of the 10 m resolution S2A product. Orbital GCC was calculated using the following sentinel-2 bands: 490 (blue-B2), 560 (green-B3) and 665 nm (red-B4), all bands with 10 m resolution. As the resolution of the NDVI MODIS product is greater than the size of the monitoring plot, only the pixel that coincided with the monitoring area was considered. We assumed that the monitoring plot is homogeneous and without border effects. In Sentinel-2 images, the pixels were cut out using the monitoring plot shape (Figure 1), and all the pixels of the monitoring plot were selected. After the central pixels representing the monitoring plot were extracted, GCC and NDVI were calculated. Next, an average of the values was extracted for the monitoring plot. Mean and standard deviation (sd) of the NDVI values for each image were calculated.

We obtained Soil-Adjusted Vegetation Index - SAVI; this concerns an improved NDVI with a soil effect factor (L). In this paper L is considered to equal 0.37 (as adjusted by (23));

$$SAVI = \frac{(1 + L)x(NIR - Red)}{L + NIR + Red} \quad [6]$$

To compare satellite data (i.e., orbital remote sensing data) with data from phenocam (i.e., near-surface remote sensing data), we calculated the SAVI, NDVI and GCC from Sentinel-2 for the tower region, where the phenocam is installed. For this calculation, a 50 m radius circle around the EC flux tower was considered as the footprint for the phenocam view.

2. Supplementary Results

Table S1 shows the fitted soil parameters for each layer. There is an apparent homogeneity in the first three layers and the maximum and minimum soil moisture content values observed for each layer indicate that this could be caused by a lack of model skill with regards to the optimization of the fitted parameters θ_s and θ_r . In fact, values of observed minimum θ values (obtained in situ) lower than the estimated θ_r values, and observed maximum θ values higher than the estimated θ_s , reveal the Durner model's inability to accurately capture the extreme ends of the water retention curve, despite the high r^2 . However, this issue is not uncommon for these kinds of models.

Table S1. Soil characteristics estimated: $\theta_s, \theta_{fc}, \theta_{wp}, \theta_r$; the θ_{max} and θ_{min} observed for each monitored soil layer depth (in $\text{cm}^3 \text{cm}^{-3}$) and; the r^2 of the Durner model versus observed water retention curve, for each layer.

Depth layer (cm)	θ_s	θ_{fc}	θ_{wp}	θ_r	θ_{max}	θ_{min}	r^2
5	0.232	0.207	0.104	5.04E-04	0.259	0.066	0.96
15	0.227	0.210	0.092	2.11E-06	0.239	0.048	0.98
25	0.227	0.213	0.107	2.12E-06	0.250	0.074	0.98
40	0.450	0.231	0.100	0.068	0.204	0.058	1.00
65	0.610	0.258	0.141	0.049	0.289	0.071	0.94

Figure S1 shows the scatter plot of measured individuals sapwood depth and DBH; the relation was used to estimate species sapwood depth. The linear regression between sapwood depth and DBH was given by $0.377 * \text{DBH} - 1.075$, R^2 of 0.67 ($p < 0.05$ for both coefficients).

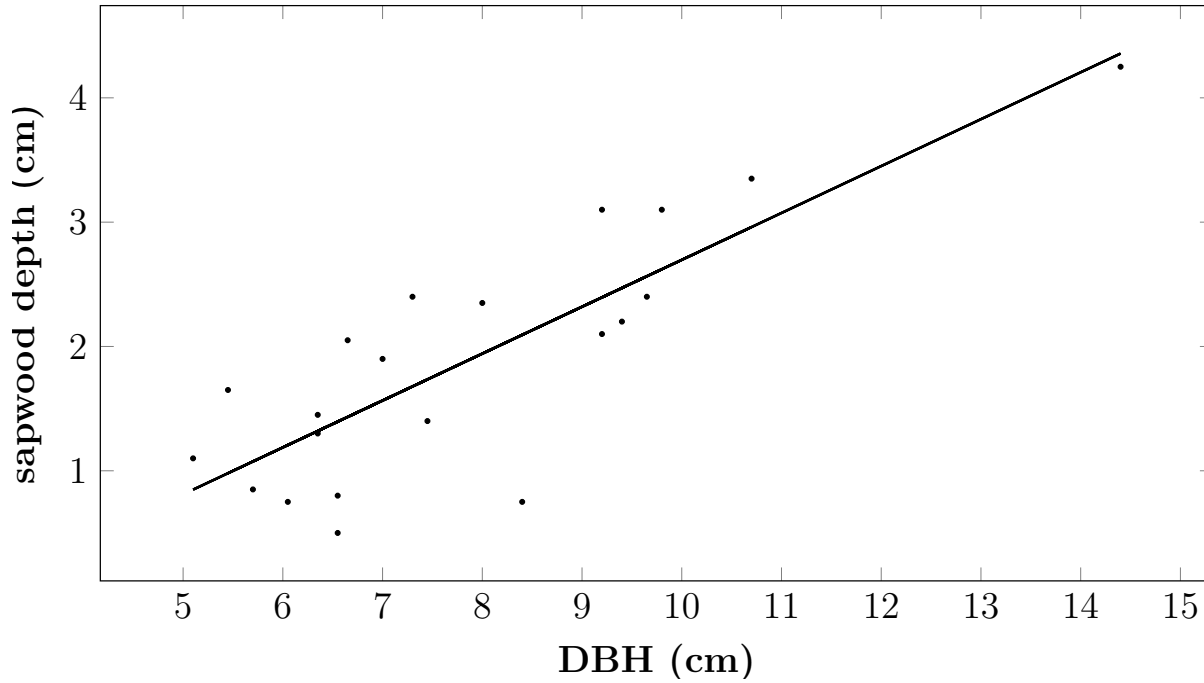


Fig. S1. Scatter plot of measured individuals sapwood depth (cm) and their respective DBH (cm).

The correlations between GCC_{ns} and orbital VIs can be found in Table S2.

Table S2. Pearson correlation table - near-surface GCC versus orbital VI

	GCC_{ns}	GCC_{S2}	NDVI_{S2}	SAVI_{S2}
GCC_{ns}	1			
GCC_{S2}	0.71	1		
NDVI_{S2}	0.72	0.98	1	
SAVI_{S2}	0.74	0.92	0.91	1
NDVI_{modis}	0.59	0.97*	1*	1

All correlations with p value < 0.01

* Correlations based on just seven matched observations

The signal evolution of VIs used compared with the evolution of F_{dnc} is given in Figure S2.

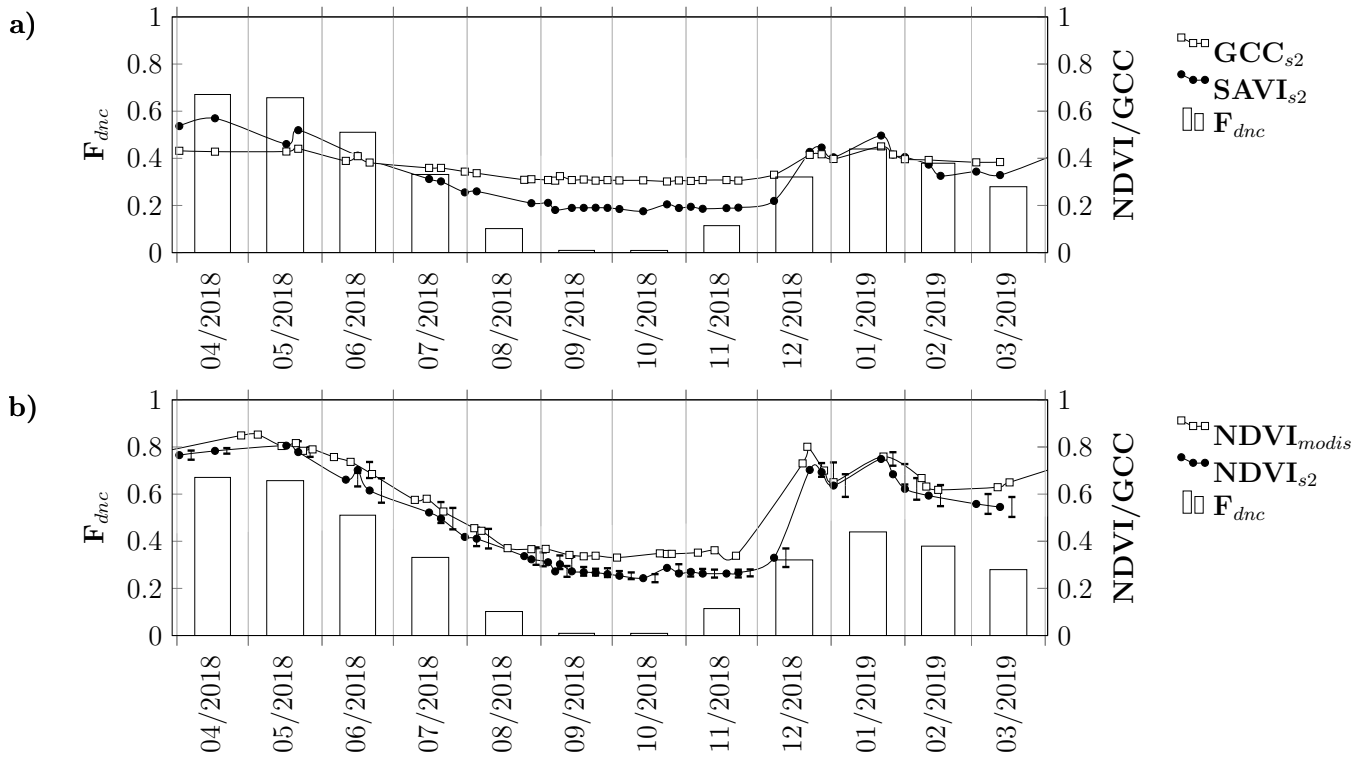


Fig. S2. Community sap flow and phenological response: A) Normalized sap flow for the plot community (F_{dnc} , dimensionless), GCC_{s2} and $SAVI_{s2}$. B) F_{dnc} , $NDVI_{modis}$ and $NDVI_{s2}$

References

1. T Wutzler, M Reichstein, AM Moffat, M Migliavacca, *REddyProc: Post Processing of (Half-)Hourly Eddy-Covariance Measurements*, (2019) R package version 1.2.
2. R Core Team, *R: A Language and Environment for Statistical Computing* (R Foundation for Statistical Computing, Vienna, Austria), (2019).
3. PF da Silva, et al., Seasonal patterns of carbon dioxide, water and energy fluxes over the Caatinga and grassland in the semi-arid region of Brazil. *J. Arid Environ.* **147**, 71–82 (2017).
4. J Topp, G.C. and Davis, A P. Annan, Electromagnetic determination of soil water content: Measurement in coaxial transmission lines. *Water Resour. Res.* **16**, 574–582 (1980).
5. I Decagon Devices, 5tm water content and temperature sensor ("http://manuals.decagon.com/Retired%20and%20Discontinued/Manuals/13441_5TM_Web.pdf") (2017) [Online; accessed 22-June-2020].
6. A Verhoef, G Egea, Modeling plant transpiration under limited soil water: Comparison of different plant and soil hydraulic parameterizations and preliminary implications for their use in land surface models. *Agric. For. Meteorol.* **191**, 22–32 (2014).
7. W Durner, Hydraulic conductivity estimation for soils with heterogeneous pore structure. *Water Resour. Res.* **30**, 211–223 (1994).
8. K Seki, Swrc fit - a nonlinear fitting program with a water retention curve for soils having unimodal and bimodal pore structure. *Hydrol. Earth Syst. Sci. Discuss.* **4**, 407–437 (2007).
9. MJ Best, et al., The joint UK land environment simulator (JULES), model description – part 1: Energy and water fluxes. *Geosci. Model. Dev.* **4**, 677–699 (2011).
10. A Granier, Une nouvelle méthode pour la mesure du flux de sève brute dans le tronc des arbres. *Annales des Sci. For.* **42**, 193–200 (1985).
11. L Ping, U Layrent, Z Ping, Granier's thermal dissipation probe (tdp) method for measuring sap flow in trees: Theory and practice. *Acta Bot. Sinica* **46**, 631–646 (2004).
12. MW Lubczynski, DC Chavarro-Rincon, DG Rossiter, Conductive sapwood area prediction from stem and canopy areas-allometric equations of kalahari trees, botswana. *Ecohydrology* **10**, e1856 (2017).
13. M Quiñonez-Piñón, C Valeo, Assessing the translucence and color-change methods for estimating sapwood depth in three boreal species. *Forests* **9**, 686 (2018).
14. B Alberton, et al., Leafing patterns and drivers across seasonally dry tropical communities. *Remote. Sens.* **11**, 2267 (2019).
15. B Alberton, et al., Introducing digital cameras to monitor plant phenology in the tropics: applications for conservation. *Perspectives Ecol. Conserv.* **15**, 82–90 (2017).

16. AD Richardson, BH Braswell, DY Hollinger, JP Jenkins, SV Ollinger, Near-surface remote sensing of spatial and temporal variation in canopy phenology. *Ecol. Appl.* **19**, 1417–1428 (2009).
17. AD Richardson, Tracking seasonal rhythms of plants in diverse ecosystems with digital camera imagery. *New Phytol.* **222**, 1742–1750 (2019).
18. H Ahrends, et al., Tree phenology and carbon dioxide fluxes: use of digital photography for process-based interpretation at the ecosystem scale. *Clim. Res.* **39**, 261–274 (2009).
19. DM Woebbecke, GE Meyer, KV Bargaen, DA Mortensen, Color indices for weed identification under various soil, residue, and lighting conditions. *Transactions ASAE* **38**, 259–269 (1995).
20. B Alberton, et al., Using phenological cameras to track the green up in a cerrado savanna and its on-the-ground validation. *Ecol. Informatics* **19**, 62–70 (2014).
21. K. Didan, Mod13q1 modis/terra vegetation indices 16-day l3 global 250m sin grid v006 (2015).
22. K. Didan, Myd13q1 modis/aqua vegetation indices 16-day l3 global 250m sin grid v006 (2015).
23. R de Queiroga Miranda, RLB Nóbrega, MSB de Moura, S Raghavan, JD Galvêncio, Realistic and simplified models of plant and leaf area indices for a seasonally dry tropical forest. *Int. J. Appl. Earth Obs. Geoinformation* **85**, 101992 (2020).